NASA

Technical Memorandum 83813

FRESNEL-REGION FIELDS AND ANTENNA NOISE-TEMPERATURE CALCULATIONS FOR ADVANCED MICROWAVE SOUNDING UNITS

R. F. Schmidt

January 1982

National Aeronautics and
Space Administration

Goddard Space Flight Center
Greenbelt, Maryland 20771

TM 83813

FRESNEL-REGION FIELDS AND ANTENNA NOISE-TEMPERATURE CALCULATIONS FOR ADVANCED MICROWAVE SOUNDING UNITS

R. F. Schmidt
NASA/Goddard Space Flight Center
Greenbelt, Maryland 20771

January 1982

GODDARD SPACE FLIGHT CENTER
Greenbelt, Maryland

FRESNEL-REGION FIELDS AND ANTENNA NOISE-TEMPERATURE CALCULATIONS FOR ADVANCED MICROWAVE SOUNDING UNITS

R. F. Schmidt
NASA/Goddard Space Flight Center
Greenbelt, Maryland 20771

ABSTRACT

This document makes a transition from the antenna noise-temperature formulation for extended noise sources in the far-field or Fraunhofer-region of an antenna to one of the intermediate near-field or Fresnel-region. The effort is directed toward microwave antenna simulations and high-speed digital computer analysis of radiometric sounding units used to obtain water vapor and temperature profiles of the atmosphere. Fresnel-region fields are computed at various distances from the aperture. The antenna noise-temperature contribution of an annular noise source is computed in the Fresnel-region ($D^2/16\lambda$) for a 13.2cm diameter offset-paraboloid aperture at 60GHz. The time-average Poynting vector is used to effect the computation.

CONTENTS

ILLUSTRATIONS

ILLUSTRATIONS (Continued)

GLOSSARY OF NOTATION

D	diameter of a circular aperture (meters)
λ	wavelength (meters)
N	exponent in feed function
C_0	range constant
$\bar{E}(x', y', z')$	electric field (volts/meter)
$\bar{H}(x', y', z')$	magnetic field (ampere-turns/meter)
j	complex operator
ω	angular frequency (radius/sec.)
f	frequency (cycles/sec.)
$\bar{n}$	surface unit normal
μ	permeability (henry/meter)
ϵ	inductive capacity (farad/meter)
∇	gradient operator (grad)
ψ	Green's function or phase (in context)
r	radial distance (meters)
ds	differential area (meters squared)
S_1, S_2	closed surfaces (in context)
k	wave number (radians/meter)
$(\hat{1}_\theta, \hat{1}_\phi, \hat{1}_r)$	spherical basis vectors
$(\hat{1}_x, \hat{1}_y, \hat{1}_z)$	Cartesian basis vectors
$\bar{K}$	sheet-current
$\langle\bar{P}\rangle$	time-average Poynting vector (watts/meter squared)
$T_A(\theta, \phi), T_A(x', y', z')$	antenna noise-temperature (deg. Kelvin)
$G_A(\theta, \phi)$	antenna directive-gain function
$d\Omega$	differential solid-angle (steradians)
$T_S(\theta, \phi), T_S(x', y', z')$	noise-temperature distribution function (deg. Kelvin)
z_0	characteristic impedance of free-space (ohms)
S	scalar feed intensity (in context)
(r, θ, ϕ)	spherical distance and angle variables (generic)
(R, Θ, Φ)	spherical distance and angle variables (feed)
$\bar{S}$	Poynting vector
(α, β, γ)	Euler angles, coefficients of $\nabla\xi$ (in context)
(x_p, y_p, z_p)	parent-paraboloid coordinates
$(\sigma_{IP}, \zeta_{IP}), (\sigma_P, \zeta_P)$	radial and azimuthal generating parameters of the offset paraboloid, and parent paraboloid
$(x_T, y_T, z_T), (x_1, y_1, z_1)$	translation parameters
(x_{PT}, y_{PT}, z_{PT})	translated parent paraboloid coordinates

FRESNEL-REGION FIELDS AND ANTENNA NOISE-TEMPERATURE CALCULATIONS FOR ADVANCED MICROWAVE SOUNDING UNITS

INTRODUCTION

An objective of this document is to effect a transition between the well-known expressions for antenna noise-temperature associated with extended noise sources in the far-field (Fraunhofer) region of an antenna and a formulation suitable for application in the intermediate near-field (Fresnel) region of an antenna. It will be shown that a simple transition can be made in a systematic manner by (1) restoring certain factors of the far-field expression which are inherent to the physical process and, (2) introducing the unambiguous time-average Poynting vector. By implication the Cartesian coordinate basis replaces the moving trihedron of the spherical basis in the Fresnel-region analysis of antenna noise-temperature. The replacement is a particularly natural one when focusing apertures (paraboloids, canonical Cassegrain and Gregorian systems, shaped dual-reflector systems, etc.) are to be dealt with since the spherical coordinate net and the Cartesian coordinate net conform to the Fraunhofer and Fresnel-region fields, respectively.

A further objective of this document is to obtain a value for the increment of antenna noise-temperature contributed by an on-board obstacle, or noise source, situated in the Fresnel-region ($D^2/16\lambda$) of the 13.2cm offset-paraboloid aperture at 5.0mm wavelength (60.0GHz). An idealized obstacle, resembling a flat washer, was selected for this calculation. The axes of rotational symmetry of the obstacle and the projected antenna aperture are congruent here. The Fresnel-region fields exhibit uniplanar symmetry. In anticipation of subsequent calculations the time-average Poynting vector components were developed over the domain $(D^2/32\lambda) \leq z_{AP} \leq (2D^2/\lambda)$, incrementing position by octaves, but only the representative cases ($D^2/16\lambda$, $D^2/8\lambda$) are illustrated here. Two illumination distributions were considered for the aperture.

The scattering formulation used in this document will now be presented as a matter of record, and to further clarify the advantage (if not outright necessity) of introducing the time-average Poynting vector for the Fresnel-region. The line of demarcation between the latter and the Fraunhofer region is somewhat imprecise. For aperture-antennas the criteria ($C_0 = 2$) in

$$R = C_0 D^2/\lambda \tag{1}$$

is frequently cited for separating the two regions. The preceding implies a phase departure of $\lambda/16$ or $\pi/8$ radians at the extreme radius of a circular cophased aperture due to the proximity of the observer. Some investigators allow a phase degradation corresponding to $C_0 = 1$, but effects can be seen in both amplitude and phase patterns of aperture antennas at either radius when making a comparison with a range corresponding to, say, $C_0 = 10$. See Ref. 1, p. 264, and Ref. 2, p. 30.

The expression (1) should be used with some discretion when dealing with antennas generally. For example, the effective diameter for a hypergoloidal subsystem of a Cassegrain configuration is zero.

THE SCATTERING FORMULATION

An amended form of the Kirchhoff-Kottler formulation, as written for perfectly conducting surfaces, was used to generate the Fresnel-region field vectors utilized in this document. It is a variant of the Stratton-Chu formula which is sometimes termed the "physical-optics" method. It suffices to illustrate the onset of certain special effects[1] as the Fresnel-region is penetrated. See Ref. 3, p. 460; Ref. 4, p. 158; Ref. 5, p. 4; Ref. 6, p. 35.

The complex-vector fields (electric and magnetic) are given by

$$\bar{E}(x', y', z') = \frac{1}{j\omega\epsilon} \frac{1}{4\pi} \int_{S_1} [(\bar{n} \times \bar{H}_1) \cdot \nabla] \nabla \psi \, ds - j\omega\mu \frac{1}{4\pi} \int_{S_1} (\bar{n} \times \bar{H}_1) \psi \, ds \tag{2}$$

[1] Departure from inverse first-order r-dependence of fields, and departure from the free-space impedance value are included.

$$\overline{H}(x', y', z') = -\frac{1}{4\pi} \int_{s_1} (\bar{n} \times \overline{H}_1) \times \nabla \psi \, ds, \tag{3}$$

where

$$\psi = \frac{e^{-jkr}}{r}, \tag{4}$$

and

$$\nabla \psi = -\left(jk + \frac{1}{r}\right) \psi \hat{1}_r. \tag{5}$$

At large distances from a scatterer or antenna there are several simplifications. Since the totality of radial field components of $\overline{E}(x', y', z')$, as well as the radial field components of $\overline{H}(x', y', z')$, vanish at infinity consistent with the Sommerfeld conditions,[1]

$$\frac{1}{j\omega\epsilon} \frac{1}{4\pi} \int_{s_1} [(\bar{n} \times \overline{H}_1) \cdot \nabla] \nabla \psi \, ds - j\omega\mu \frac{1}{4\pi} \int_{s_1} \overline{K}_{1_r} \psi \, ds = 0. \tag{6}$$

This is predicated on the resolution of sheet current into radial and transverse components with respect to radial vector $(\hat{1}_r)$:

$$(\bar{n} \times \overline{H}_1) = \overline{K}_1 = \overline{K}_{1_r} + \overline{K}_{1_t}. \tag{7}$$

Then

$$\overline{E}(x', y', z') = -j\omega\mu \frac{1}{4\pi} \int_{s_1} \overline{K}_{1_t} \psi \, ds. \tag{8}$$

Even though $(\bar{n} \times \overline{H}_1) \times \nabla \psi$ in $\overline{H}(x', y', z')$ is necessarily transverse, and the latter is therefore also transverse, this observation does not assist in the evaluation of the ratio $|\overline{E}(x', y', z')|/|\overline{H}(x', y', z')|$. Proceeding analogously, as with the treatment of the electric field,

$$\overline{H}(x', y', z') = -\frac{1}{4\pi} \int_{s_1} \overline{K}_{1_t} \times \nabla \psi \, ds \tag{9}$$

[1] See also Appendix A, where the radia. lectric field at infinity is shown to vanish without resorting to the Sommerfeld conditions.

since

$$\overline{K}_{1_r} \times \nabla \psi \equiv 0 \tag{10}$$

for all

$$\overline{K}_{1_r} \not\equiv 0 \tag{11}$$

due to the parallelism

$$\overline{K}_{1_t} \parallel \nabla \psi. \tag{12}$$

Now the orthogonal relationship

$$\overline{E}(x', y', z') \perp \overline{H}(x', y', z') \tag{13}$$

holds, and the fields are seen to be temporally synchronous.

From the preceding development,

$$\frac{|\overline{E}(x', y', z')|}{|\overline{H}(x', y', z')|} = \frac{|-j\omega\mu \left(\frac{1}{4\pi}\right) \int_{S_1} \overline{K}_{1_t} \psi \, ds|}{|-\left(\frac{1}{4\pi}\right) \int_{S_1} \overline{K}_{1_t} \times \nabla \psi \, ds|} = \frac{|j\omega\mu \int_{S_1} \overline{K}_{1_t} \psi \, ds|}{|jk \int_{S_1} \overline{K}_{1_t} \psi \times \hat{1}_r ds|} = \frac{\omega\mu}{k} = \sqrt{\frac{\mu_0}{\epsilon_0}} = z_0 \tag{14}$$

in free-space since the operation $\overline{K}_{1_t} \times \hat{1}_r$ rotates all of the vectors $\overline{K}_{1_t}$ by 90-degrees, spatially, and since

$$\overline{K}_{1_t} \times \hat{1}_r = |\overline{K}_{1_t}| \, |\hat{1}_r| \sin \angle(\overline{K}_{1_t}, \hat{1}_r \hat{1}_t') = |\overline{K}_{1_t}| \hat{1}_t' \tag{15}$$

and

$$\lim_{r \to \infty} -\left(jk + \frac{1}{r}\right) \psi \hat{1}_r = -jk \, \psi \hat{1}_r. \tag{16}$$

It is noted that $\overline{K}_{1_t}$ is the component of $\overline{K}_1$ which is transverse to radial vector $(\hat{1}_r)$. Here $(\hat{1}_t')$ is transverse to both $(\hat{1}_t)$ and $(\hat{1}_r)$.

THE TIME-AVERAGE POYNTING VECTOR

The preceding section on the scattering formulation established the fact that the radiative fields ($r \to \infty$) are both spatially orthogonal and temporally synchronous. This observation is

relevant with regard to the time-average Poynting vector. See Ref. 3, p. 137; Ref. 7, p. 313; Ref. 8, p. 322:

$$<\overline{P}> = \frac{1}{2} \text{Re } \overline{E} \times \overline{H}^* \quad \text{w/m}^2. \tag{17}$$

In (17), the vector cross-product and introduction of the conjugation constitute spatial and temporal projections, respectively. This is easily verified by such simple tests as assuming $\overline{E} \perp \overline{H}$, $\overline{E} \parallel \overline{H}$, $\overline{E} \rightarrow \overline{E} \angle\psi_E$, $\overline{H} \rightarrow \overline{H} \angle\psi_E$, $\overline{H} \rightarrow \overline{H} \angle\psi_{E+\pi/2}$, etc. in various permutations.

By implication there may then exist, in certain regions about a scatterer of electromagnetic fields, components of fields which do not contribute to radiation. The underlying reason may be spatial parallelism, or temporal quadrature, or both. In a generic situation, the appropriation of such electric or magnetic field distributions as $\overline{E}(\theta, \phi)$, $\overline{H}(\theta, \phi)$ to form directive gain functions $G(\theta, \phi)$ may at times be in error. The time-average Poynting vector is a combination of six magnitudes and six phase values, which leads to a single complex-vector for every point in space where the fields are defined and, via a double-projection, remains free of error with regard to radiated power-density. This vector may be variously directed, but it always extracts the space-time relationship between the electric and magnetic fields that is exhibited in the Sommerfeld far-field conditions in forming the magnitude $|<\overline{P}>|$.

THE ANTENNA NOISE-TEMPERATURE FORMULATION

Ordinarily the far-field radiation pattern of an antenna is used for the calculation of antenna noise-temperature in a cross-correlation with a brightness distribution over some solid angle (often 4π steradians.) Both $T_s(\theta, \phi)$ and $G_A(\theta, \phi)$ may be visualized as lying on concentric spheres of equal radii, which are free to move with respect to one another. The associated equations usually appear as

$$T_A(\theta, \phi) = \frac{\iint_{4\pi} T_s(\theta, \phi)\, G_A(\theta, \phi)\, d\,\Omega}{\iint_{4\pi} G_A(\theta, \phi)\, d\,\Omega}, \tag{18}$$

and

$$T_A(\theta, \phi) = \iint_{4\pi} T_s(\theta, \phi)\, G_A(\theta, \phi)\, d\,\Omega, \tag{19}$$

where power-normalization has been effected in the latter case. See Ref. 1, p. 372; Ref. 9, p. 150.

The expressions for antenna noise-temperature, (14) and (15) above, appear independent of range (r) when far-field or Fraunhofer conditions are assumed to exist, but these equations may be rewritten to advantage by introducing the r-dependence of $G_A(r, \theta, \phi)$ and differential area $ds(r, \theta, \phi)$. From the definition of solid angle, Ref. 10, p. 290,

$$d\,\Omega = \frac{\overline{r} \cdot \overline{n}}{r^3}\, ds \tag{20}$$

and, for the spherical coordinate system which conforms to the disposition of the physical radiation fields,

$$ds = r^2 \sin\theta\, d\,\theta\, d\,\phi. \tag{21}$$

The radiation fields are conveniently resolved into spherical components E_θ and E_ϕ, with $E_r \equiv 0$.

Since, in the Fraunhofer-region,

$$\frac{G_A(\theta, \phi)}{r^2\, z_0} = \frac{G_A(r, \theta, \phi)}{z_0} \propto \frac{E^2(r, \theta, \phi)}{2z_0}, \tag{22}$$

and since, for spatially orthogonal and temporally synchronous fields,[1]

$$|\langle \overline{P} \rangle| = \frac{1}{2} \text{Re}\,[|\overline{E}|\,|\overline{H}|\,(\underline{/\psi})\,(\underline{/-\psi})\,\sin\underline{/\overline{E},\overline{H}}] = \frac{EH}{2} = \frac{E^2}{2z_0}, \tag{23}$$

[1] It is tacitly assumed here that, following Stratton, et al., the fields are temporally sinusoidal for the Poynting vector discussion and $\overline{E}$ implies maximum-value, accounting for the factor (1/2) in equation (23).

equation (14) may be rewritten as

$$T_A(x', y', z') = \frac{\iint_S T_s(x', y', z') < \overline{P}(x', y', z') > \cdot \overline{n}\, ds}{\iint_S < \overline{P}(x', y', z') > \cdot \overline{n}\, ds} \tag{24}$$

Although (18) is recoverable from (24) and the latter is valid at all distances from the scatterer, its Cartesian form does not conform to spherical waves. It is, however, ideally suited to the Fresnel-region of an aperture antenna for which power is strongly collimated. Furthermore, the formulation (24) is also valid in a region where $(\overline{E})$ and $(\overline{H})$ fields may no longer be orthogonal or synchronous, and where (E^2) or (H^2) may no longer be a valid measure proportional to power (P) since

$$\frac{|\overline{E}|}{|\overline{H}|} \neq z_0 \tag{25}$$

is possible in that region.

RECIPROCITY AND COHERENCE

The antenna noise-temperature figures generated for the example of this document were predicated on several assumptions, including

(1) The "transmit" patterns or Poynting vectors of the Fraunhofer and Fresnel-regions may be utilized for the "receive" case under the Lorentz reciprocity theorem. See Ref. 12, p. 44.

(2) The "transmit" patterns or Poynting vectors of the Fraunhofer and Fresnel-regions, whose derivation is predicated on total coherence, may be cross-correlated with a noise-temperature distribution which is associated with an incoherent source.

(3) The "transmit" patterns are affected by the specification of the feed-horn characteristics. In particular, the directivity of the prime-feed pattern, controlled by the factor (N) in the electric-field expression

$$E_{\mathcal{F}} = S \cos^N \Theta, \tag{26}$$

is a parameter affecting the Fresnel-region pattern.

It is noted that the fundamental expression for antenna noise-temperature, (18), incorporates directive-gain and is devoid of phase considerations. In analysis

$$G_A(\theta, \phi) \propto |\overline{E}(\theta, \phi) \underline{/\psi_E}|^2 \tag{27}$$

and the phase pattern, which had its origin in the assumption of a monochromatic source under an algorithm such as the physical-optics or Kirchhoff-Kottler formulation, is simply deleted.

It is interesting to examine the Poynting vector approach of the present document in this context. From (17) it can be seen that the definition of the time-average Poynting vector precludes the possibility of having phase appear in the formulation. This would not have been true if the classical Poynting vector

$$\overline{S} = \overline{E} \times \overline{H} \tag{28}$$

of Ref. 3, p. 132 had been used. Retention of explicit normalization would then have removed radiation pattern phase from the discussion however, as can be seen from an inspection of (24), assuming T_s is a constant.

RADIOMETER/NOISE-SOURCE/FIELD SYMMETRY

The assumed geometry of the advanced microwave sounding unit and the antenna noise-temperature source, a distance of $\left(\frac{D^2}{16\lambda}\right)$ away from the antenna aperture plane, are shown in Fig. 1. A scale drawing of the offset antenna alone is given as Fig. B-1. It can be seen from these figures that there is a common axis of symmetry for the circular aperture (AP) and the source of antenna noise-temperature (T_s), but only uniplanar symmetry (xz) for the time-average Poynting vectors $< \overline{P} >$ in the present calculation. The radii (σ) of the noise source are changed progressively by one-wavelength increments, increasing the outer radius and decreasing the inner radius as suggested by Fig. 1. This flat or open-surface noise source is a convenient abstraction for exploring the antenna noise-temperature increment due to an on-board source situated in the

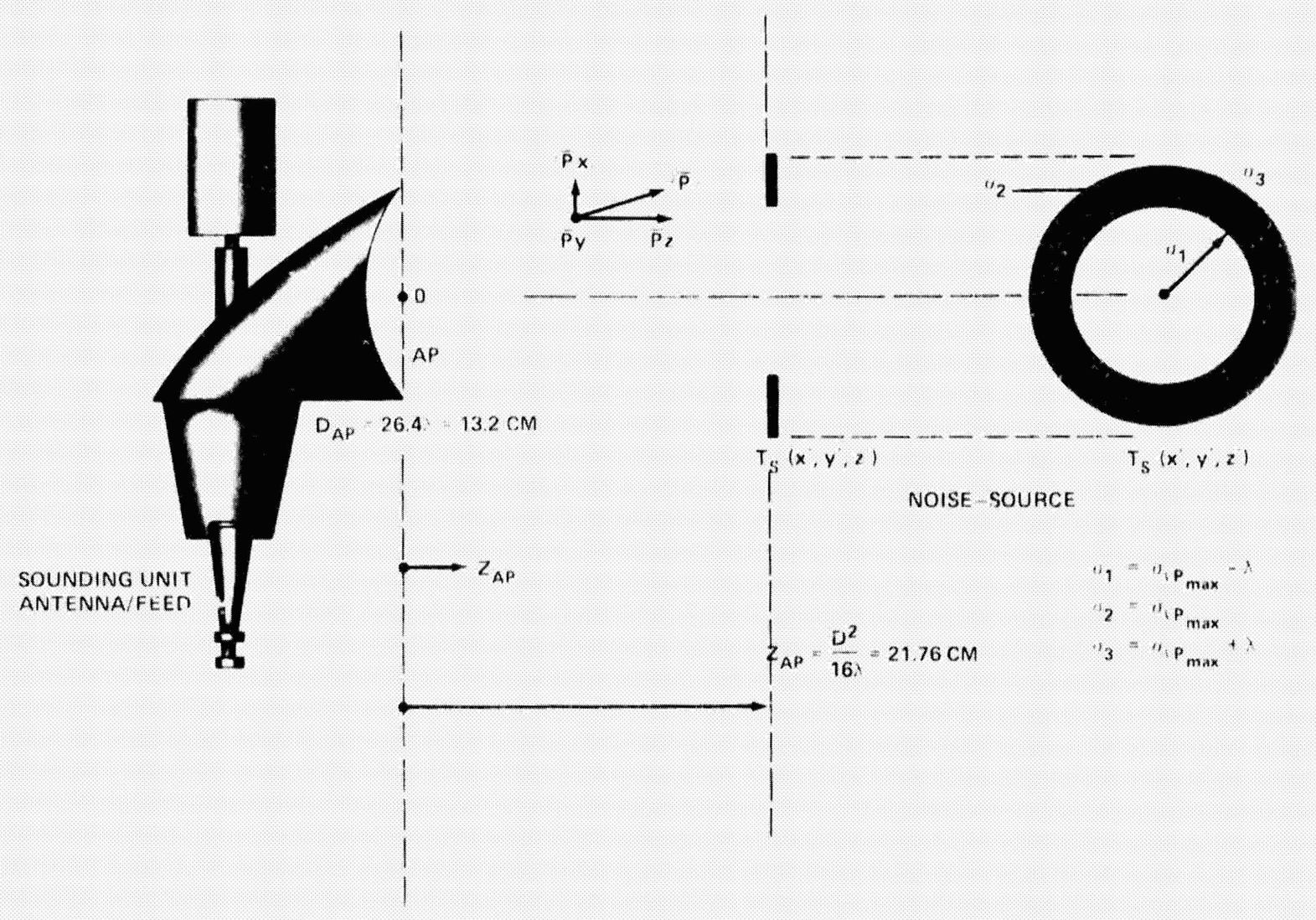

Figure 1. Radiometer Geometry.

Fresnel-region of the antenna. It can be seen that increasing the source radius away from the projected aperture radius intercepts the weak fringe radiation while decreasing the source radius away from the projected aperture radius intercepts the strongly collimated radiation of the focal-point fed paraboloid. (The "transmit" point-of-view is retained for the present discussion.) Less abstract situations, including multiple noise sources, are discussed in the closing sections of this document.

Attention is directed to the Cartesian coordinate system inferred by Fig. 1 and Fig. B-1. It is a "right-handed" system with origin at the center of the aperture (AP). All subsequent graphs and calculations adhere to this set of conventions. The fringe vectors adjacent to the strongly collimated portion of Fresnel-region will be made up of weak (Px), (Py), and (Pz) components of the time-average Poynting vector. Intuitively, the (Pz) component of $< \overline{P} >$ should be dominant inside the collimated region and raises the possibility of simplifying the computation of antenna noise-temperature in the Fresnel-region through a discreet choice of closed surface (s) in (24).

Equation (24) indicates integration over the same closed surface for both numerator and denominator. Considerable arbitrariness exists here and although the same symbol (s) is used for the closed surface, several alternatives are available. In a far-field or Fraunhofer noise-temperature calculation a large, ideally infinite, sphere encloses the antenna system. The denominator of (24) may, conceptually at least, be evaluated by integrating the directive gain function $G(\theta, \phi)$ over 4π steradians of solid-angle. As practical difficulties arise in either calculating $G(\theta, \phi)$ over all space, or measuring the same, the alternative of evaluating the denominator by integrating the time-average Poynting vector over the antenna aperture becomes attractive. It is irrelevant, therefore, whether the noise-temperature calculation happens to lie in the Fraunhofer or Fresnel domain when considering the evaluation of the denominator of (24). The closed surface may be a cylinder (s_1).

In Fig. 2 forward radiation is through the antenna aperture (AP), designated surface (I), backward radiation is through an identical area (VII), and closure is achieved with the cylindrical wall surface (VI). It may, at times, be advantageous to select a surface parallel to the aperture, but somewhat away from the radiating surface, to obviate certain computational difficulties ($r = 0$) with regard to the Green's function (4). In any event, the total radiated power flowing away from the antenna is evaluated, and the value of the denominator is invariant with respect to distance from the radiator and the shape of the closed surface (s_1).

In an analogous manner a second cylinder, (s_2) in Fig. 2, is well suited to the present noise-temperature calculations in view of the common axial symmetry of the aperture and the noise source. This surface is composed of the antenna aperture (AP), designated (I), an annular surface (II), a cylindrical wall surface (III), another annular surface (IV) associated with the physical surface of (T_s), and the interior of that annulus (V). It is noted that the unit normal ($\overline{n}$) is everywhere directed outwards to the closed surface on which the noise-temperature distribution $T_s(x', y', z')$ resides, therefore the outward normal of (s_1) on subsurface (I) must be reversed for this part of (s_2). It is also noted that the radius of the area designated (I) determines the geometric bound of the collimated energy. This energy is seen to convert from plane-wave to spherical wave in the present calculations in the manner suggested by the Poynting vectors shown in Figure 2, but it would not diverge under ray-optics (Snell's Law).

Equation (24) may be rewritten in terms of open integrals as

$$T_A(x', y', z') = \frac{\iint_{I+II+III+IV+V} T_s(x', y', z') < \overline{P}(x', y', z') > \cdot \overline{n}\, ds}{\iint_{I+VI+VII} < \overline{P}(x', y', z') > \cdot \overline{n}\, ds} \qquad (29)$$

Since (T_s) is taken to be identically zero over I, II, III and V of (s_2), and since $< \overline{P} >$ is taken to be zero over VI and VII of (s_1), (29) reduces to

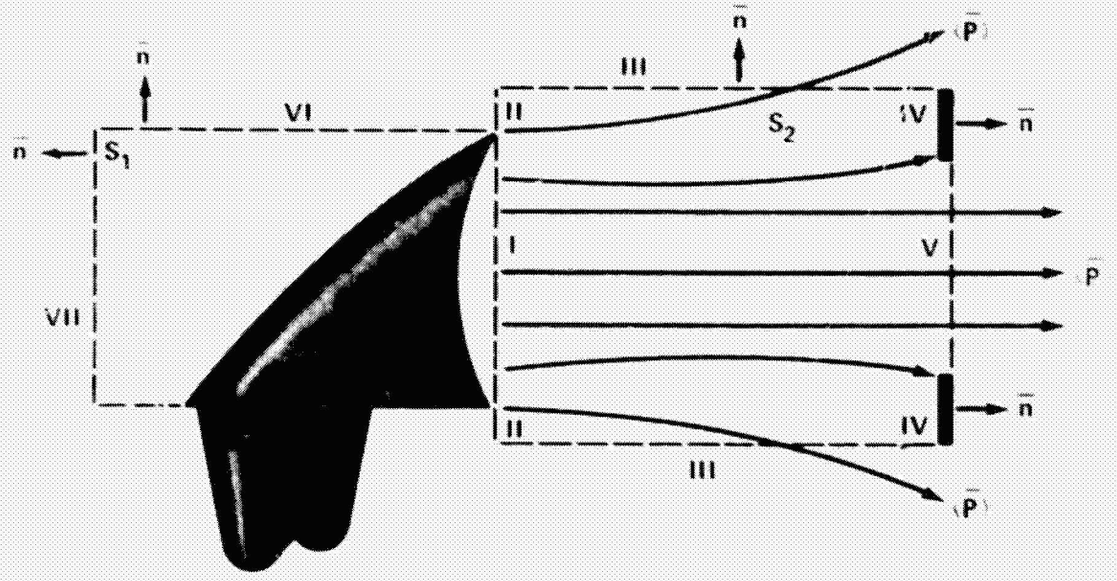

Figure 2. Closed Surfaces of the Noise-Temperature Integrals.

$$T_A(x', y', z') = \frac{\iint_{IV} T_s(x', y', z') < \bar{P}(x', y', z') > \cdot \bar{n}\, ds}{\iint_{I} < \bar{P}(x', y', z') > \cdot \bar{n}\, ds} \tag{30}$$

Now $< \bar{P}(x', y', z') >$ over IV and I are distinct. The outward normals are

$$\bar{n}_{IV} = \bar{n}_I = (0, 0, 1) \tag{31}$$

in analogy with the far-field or Fraunhofer calculation, and $T_s(x', y', z')$ is taken to be a constant here. From this it follows that

$$T_A(\sigma, \zeta) = \frac{T_s(\sigma, \zeta) \iint_{IV} P_z(\sigma, \zeta)\, \sigma\, d\, \sigma\, d\, \zeta}{\iint_{I} P_z(\sigma, \zeta)\, \sigma\, d\, \sigma\, d\, \zeta}, \tag{32}$$

after introducing the cylindrical coordinates which conform to the noise-source and antenna-aperture axial symmetry. The limits for these integrals are as follows:

$$\int_{\zeta = 0}^{2\pi} \int_{\sigma min\ (T_s)}^{\sigma max\ (T_s)}$$

and

$$\int_{\zeta = 0}^{2\pi} \int_{\sigma_0 = 0}^{\sigma max\ (AP)}$$

for integrals (IV) and (I), respectively.

Asymmetrical values for some azimuthal cuts in the plane

$$z = D^2/16\lambda \tag{33}$$

are anticipated. If half-planar cuts are deemed axially symmetric in all cases, an interpolation technique emerges. Each half-planar cut may be rotated through 2π radians, and $P_z(\sigma, \zeta)$ goes over to $P_z(\sigma)$. The open surface integral is replaced by two sets of open line integrals.

$$T_A(\sigma,\zeta) = T_s(\sigma,\zeta)\,\frac{\left(\frac{1}{m}\right)\sum_{1}^{m}\int_{\sigma\min(T_s)}^{\sigma\max(T_s)} P_m(\sigma)\,\sigma\,d\sigma}{\left(\frac{1}{n}\right)\sum_{1}^{n}\int_{0(AP)}^{\sigma\max(AP)} P_n(\sigma)\,\sigma\,d\sigma} \tag{34}$$

where the subscript (z) has been dropped since (32) has been given. There are two sets of line integrals since $P_{z_m}(\sigma)$ at the noise source and $P_{z_n}(\sigma)$ at the aperture may have completely different characteristics requiring more or less "interpolation". In either case, however,

$$\sigma = (x^2 + y^2)^{1/2}. \tag{35}$$

The line integrals of (34) may become summations over ($\Delta\sigma$). Then

$$T_A(\sigma,\zeta) = T_s(\sigma,\zeta)\,\frac{\left(\frac{1}{m}\right)\left(\frac{1}{p}\right)\sum_{1}^{m}\sum_{1}^{p} P_{mp}(\sigma)\,\sigma\,\Delta\sigma}{\left(\frac{1}{n}\right)\left(\frac{1}{q}\right)\sum_{1}^{n}\sum_{1}^{q} P_{nq}(\sigma)\,\sigma\,\Delta\sigma}. \tag{36}$$

That is, there are (m) and (n) half planar cuts for the Fresnel-region data at the noise-temperature source and at the aperture, respectively. Each of these corresponds to some azimuthal value (ζ). Each half-planar cut relates (P_z) in a one-to-one manner with some value of (σ). Each half-planar cut at the noise source and the aperture is subdivided into (p) and (q) intervals, respectively, for numerical integration purposes.

The manner of obtaining and presenting the Fresnel-region data is now detailed since this topic is closely related to the radiometer's geometrical symmetry. Figure 3 is an isometric sketch of the antenna aperture and observer loci which include points lying in the noise source. Since the offset antenna surface is derived from a parent paraboloid, axial symmetry is replaced by uniplanar symmetry. Even though the feed is circularly symmetric with respect to amplitude and phase, the polarization aspects also indicate uniplanar field symmetry with feed Euler angles $\alpha = 90°$, $\beta = 90°$, $\gamma = 0°$ and $\overline{p}_\epsilon = 0$, prior to system translation. Attention is also called to the

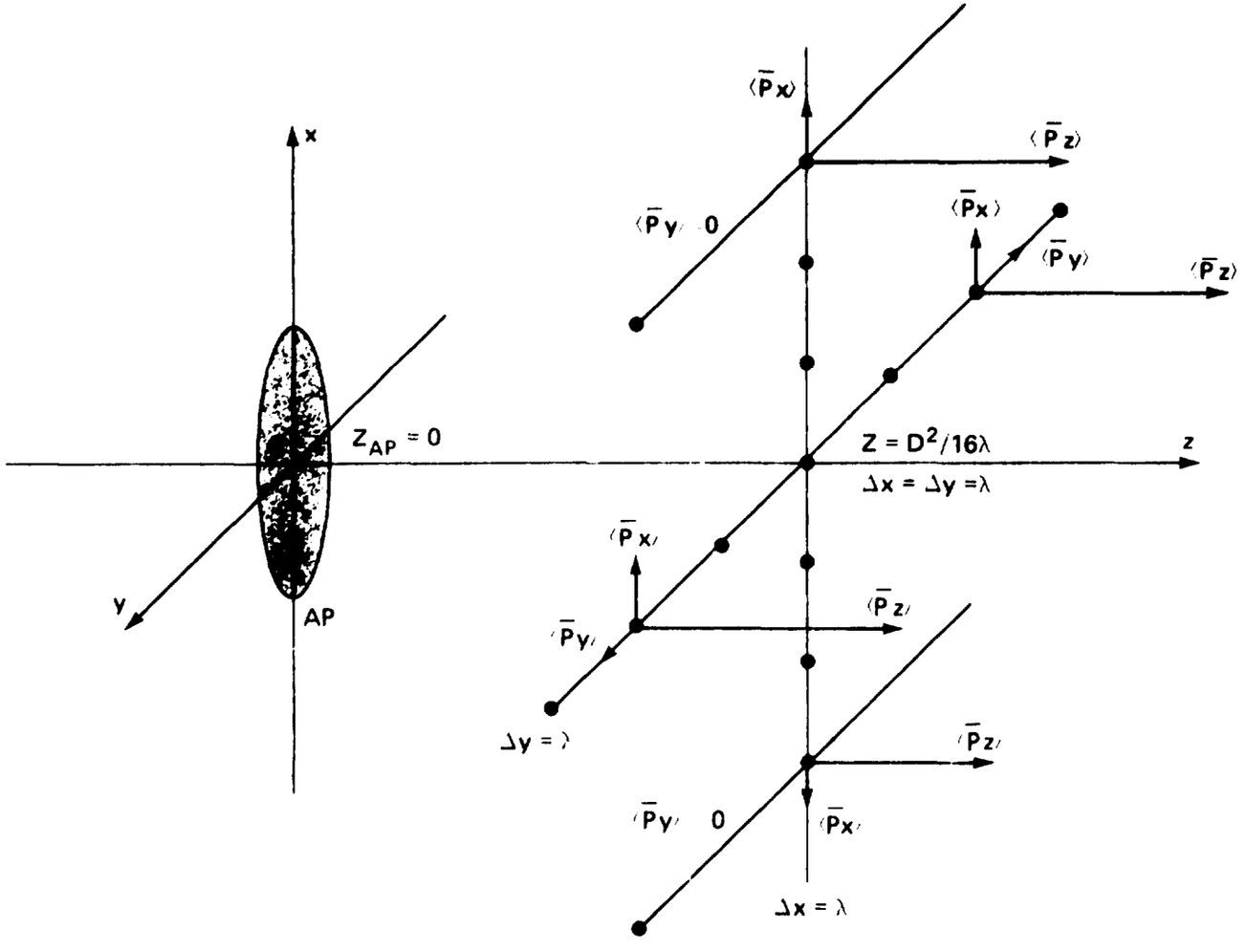

Figure 3. Loci of Observation in the Fresnel Region.

differential divergence of the prime-feed fields, which also forces uniplanar symmetry. See Fig. B-1, for which

$$dB_{max} = 20 \log (\rho_2/\rho_1) \tag{37}$$

although the latter is partially compensated by the feed pattern ($\theta_2 = 21°$, $\theta_1 = 25°$).

Figure 3 is intended to illustrate what may be anticipated from symmetry arguments alone, prior to obtaining diffraction-pattern data with a computer program. Uniplanar symmetry dictates the following:

$x = 0, \Delta y_1 = | - \Delta y_2 |, z = \text{constant}$

(1) The components of $< \overline{P}_x >$ are always codirectional and equal.

(2) The components of $< \overline{P}_y >$ are always antidirectional and equal.

(3) The components of $< \overline{P}_z >$ are always codirectional and equal.

$\Delta x_1 = | - \Delta x_2 |, y = 0, z = \text{constant}$

(4) The components of $< \overline{P}_x >$ may be co- or antidirectional, and either equal or unequal.

(5) The components of $< \overline{P}_y >$ are identically zero.

(6) The components of $< \overline{P}_z >$ may be co- or antidirectional, and either equal or unequal.

POWER-DENSITY COMPONENTS (N = 20.84)

A discussion of near-zone, intermediate near-zone (Fresnel) and far-zone (Fraunhofer) fields is found in Ref. 4, pp. 169–175. In addition, a set of graphs is given in that source showing the transition from Fresnel to Fraunhofer diffraction for a 5-wavelength slot. The author (S. Silver) refers to a column of energy propagated geometrically near the aperture (i.e., collimated power-density) and progressive diffusion of the field into the shadow region (i.e., a transition from restricted plane-wave type propagation to spherical-wave radiation). Reference 11, p. 50–51, furnishes some discussion with respect to the transmit and receive points of view in the aperture region.

The present treatment of the offset paraboloid deals with a considerably more complicated situation. As previously mentioned, only uniplanar symmetry exists due to the offset geometry as well as the prime-feed characteristics. Also, a full three-dimensional formulation is carried in terms of the Poynting vector. Another distinction is that, in the absence of any specific information to the contrary, it must be assumed that the amplitude of the aperture distribution of the example of Ref. 4 is uniform. In the present example, the feed characteristics and the interaction of the polarized incident wave with the reflector affect the aperture distribution that generates the Fresnel-region fields.

The x, y, and z components of the Poynting power-density vectors of the 13.2cm offset paraboloid are given in Figs. 4 and 5 and correspond to a 15.0dB feed edge-taper illumination at $D^2/16\lambda$ and $D^2/8\lambda$, respectively. The conclusions previously reached from regarding the symmetry of the antenna system (reflector and feed) are borne out by the computer data contained in these figures. P_x and P_z are even functions, P_y is an odd function. Rapid fluctuations are seen to exist between the two values of (z) at which the data were obtained, which is characteristic and definitive for the Fresnel-region. It is noted that the P_z plot at $z = D^2/8\lambda$ shows a tendency toward bifurcation whereas the P_z plot at $z = D^2/16\lambda$ shows a weak tendency to form a coherent beam, and further displays the oscillatory nature of the Fresnel-region. Figs. 4 and 5 also show the sharp, nearly-geometrical cutoff of the power-density vectors outside of the geometrical bounds of the projected aperture. Also of interest is the relative intensity between the maximum values of the P_x, P_y and the P_z components: approximately 20 decibels. The overall impression created by these figures is one of strong, but unstable or oscillatory, collimation in the $(\hat{1}_z)$ direction.

Figures 6 and 7, corresponding to a 0.0dB feed edge-taper illumination at $D^2/16\lambda$ and $D^2/8\lambda$, respectively, serve to illustrate the influence of the feed directivity on the Fresnel-region intensities. As before, the predicted symmetry effects may be verified, and the cutoff is sharp at the

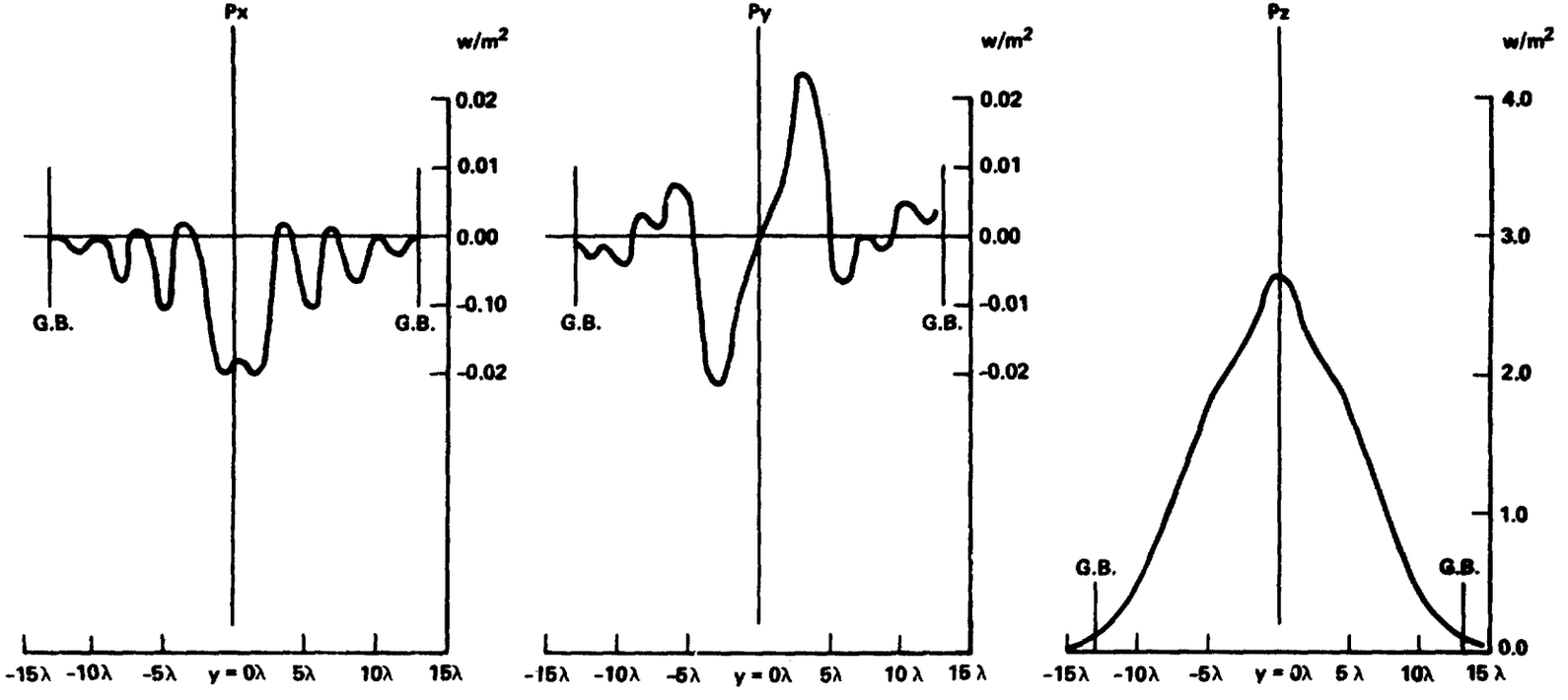

Figure 4. Power-Density Components (N = 20.84) @ Z = $D^2/16\lambda$ = 0.714 Feet.

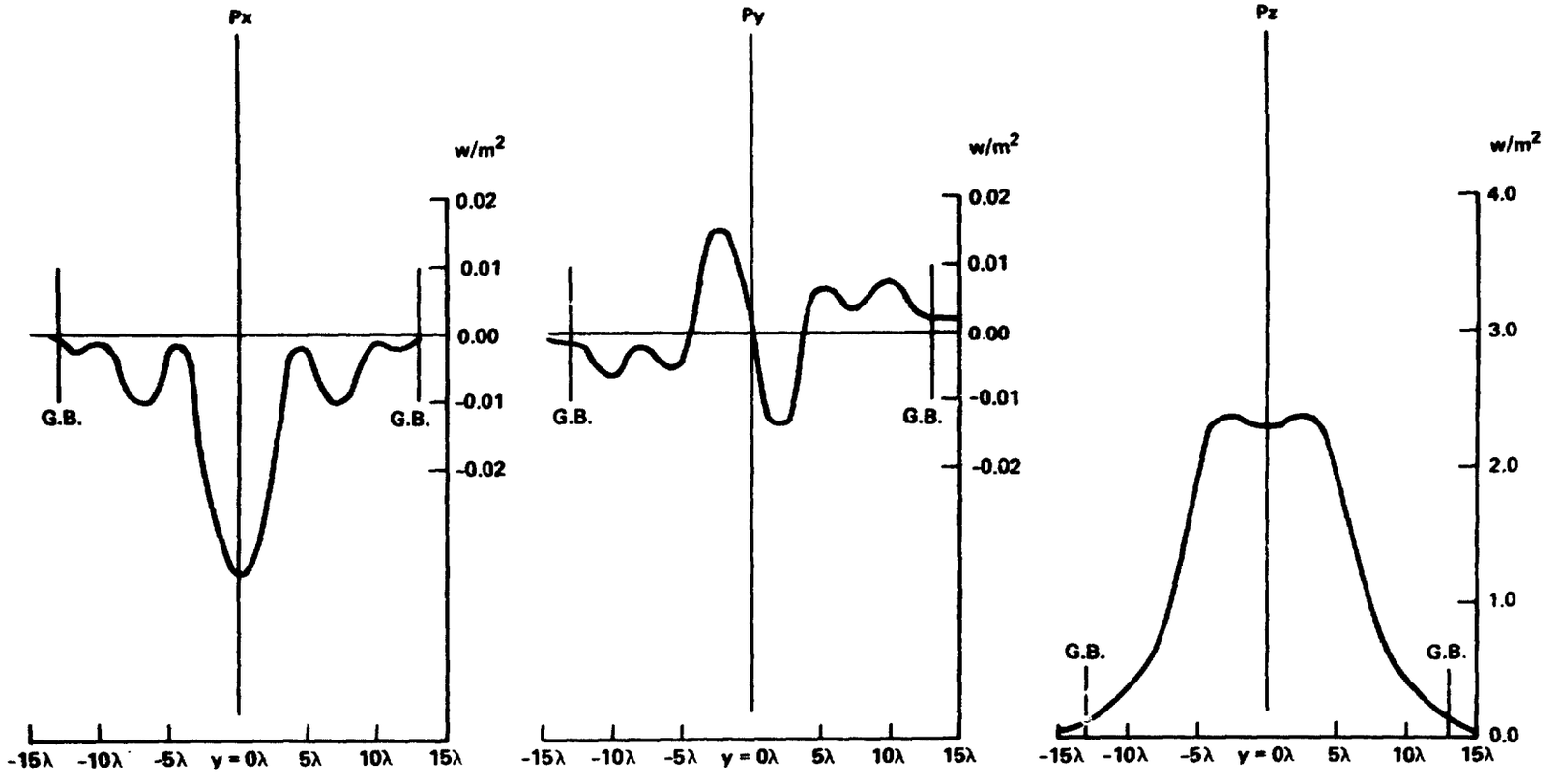

Figure 5. Power-Density Components (N = 20.84) @ $Z = D^2/8\lambda = 1.43$ Feet.

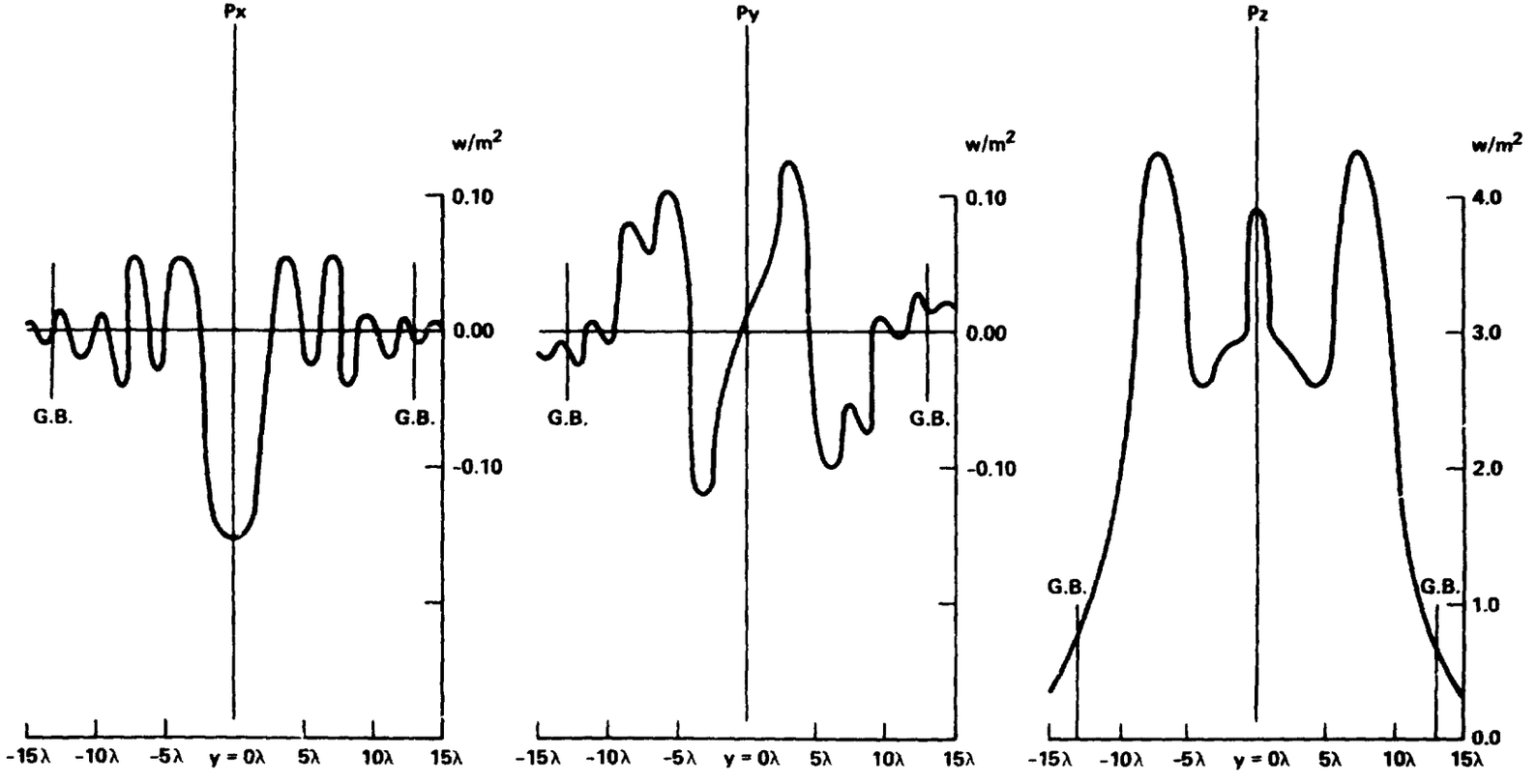

Figure 6. Power-Density Components (N = 20.84) @ Z = $D^2/16\lambda$ = 0.714 Feet.

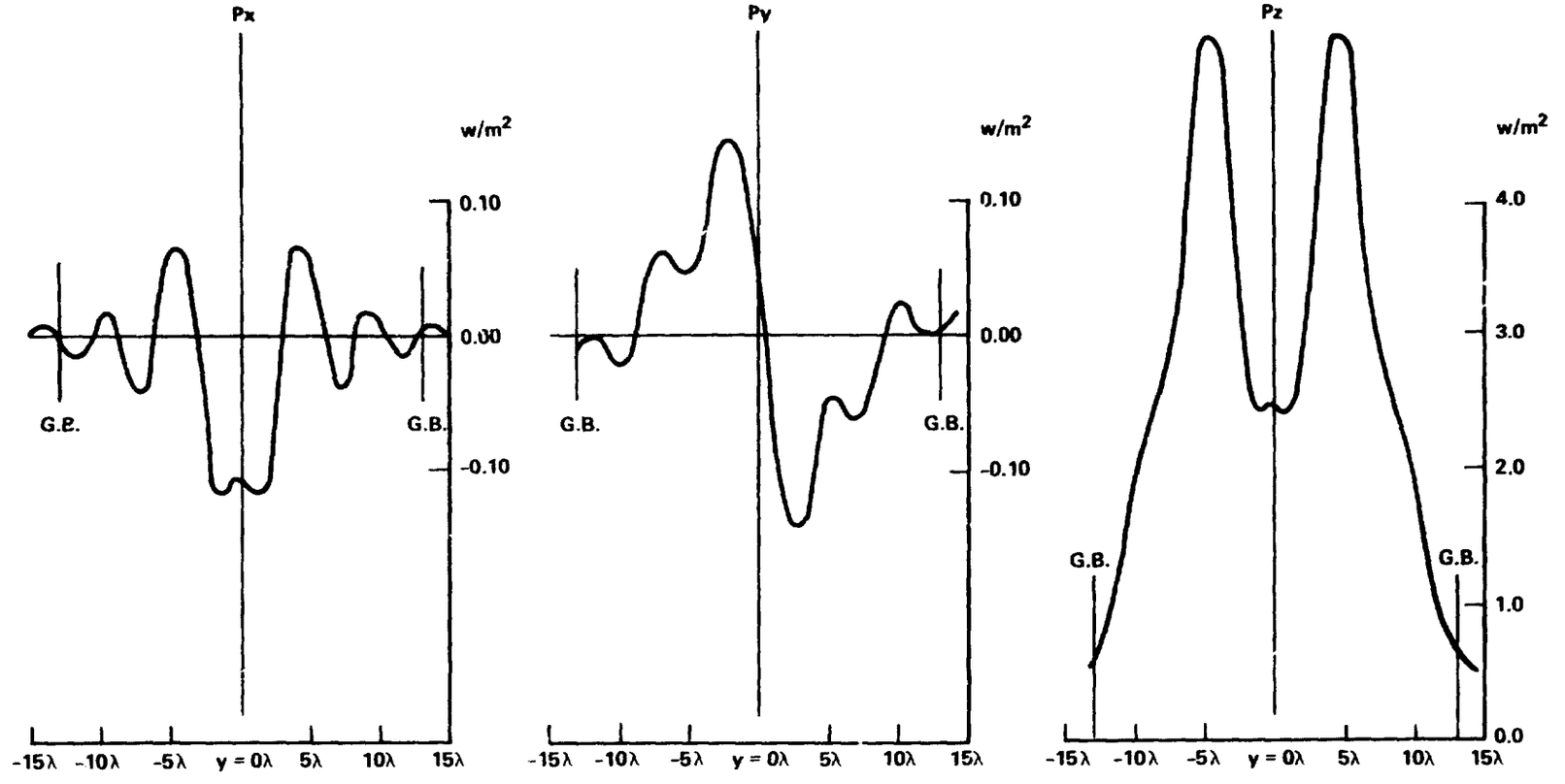

Figure 7. Power-Density Components (N = 0.00) @ $Z = D^2/8\lambda = 1.43$ Feet.

geometric bound of the projected aperture. The relative intensity between the maximum values of P_x, P_y and the P_z components is now approximately 16 decibels.

Figure 8 is a composite plot of the data obtained along the lines with slope m = 0, 1, ∞ in the xy-plane, $z = D^2/16\lambda$, with N = 20.84. The asymmetrical nature of this result obviously requires some interpolation scheme so that the noise-temperature calculation will be meaningful. Equation (37) was developed for dealing with a (P_z) distribution such as that shown in Fig. 8, where only a finite number of cuts was available, and where each of these cuts provided a certain number of data points depending on a chosen increment ($\Delta\sigma$).

A summary of the effects observed for the other traverses through the Fresnel-region ($D^2/32\lambda \leq z \leq 2D^2/\lambda$ by octaves) is given in lieu of additional plots similar to Fig. 4 through 7. It was found that, in all cases, the highly oscillatory nature of the three components of $<\overline{P}>$ vanished for values of z greater than $D^2/4\lambda$ over the 30λ domain of (σ) explored here. The values of (P_x) and (P_y) tended toward zero, and the appearance of energy outside of the geometric bound increased rapidly for z greater than D^2/λ. It is recalled that

$$BW^{\circ}_{-3\,dB} \approx \frac{70\lambda}{D}. \tag{38}$$

so that the half angle

$$\Theta/2_{-3\,dB} \approx 1.3^{\circ} \tag{39}$$

for the 13.2cm aperture at 60GHz. For N = 20.84, N = 0.00, the -3dB level lies outside of the geometric bound and beyond $\sigma max = 30\lambda$ for $z = 2D^2/\lambda$. An extrapolation to the -3dB level for N = 0.00 was made, with a resulting estimate that

$$\Theta/2_{-3\,dB} \approx 1.4^{\circ}, \tag{40}$$

which is reasonable compared to the result of the approximation formula (38).

It is noted that the oscillatory character of the Fresnel-region fields, particularly in the (P_z) component, may be exploited in physical situations. For example, an inspection of the numerous

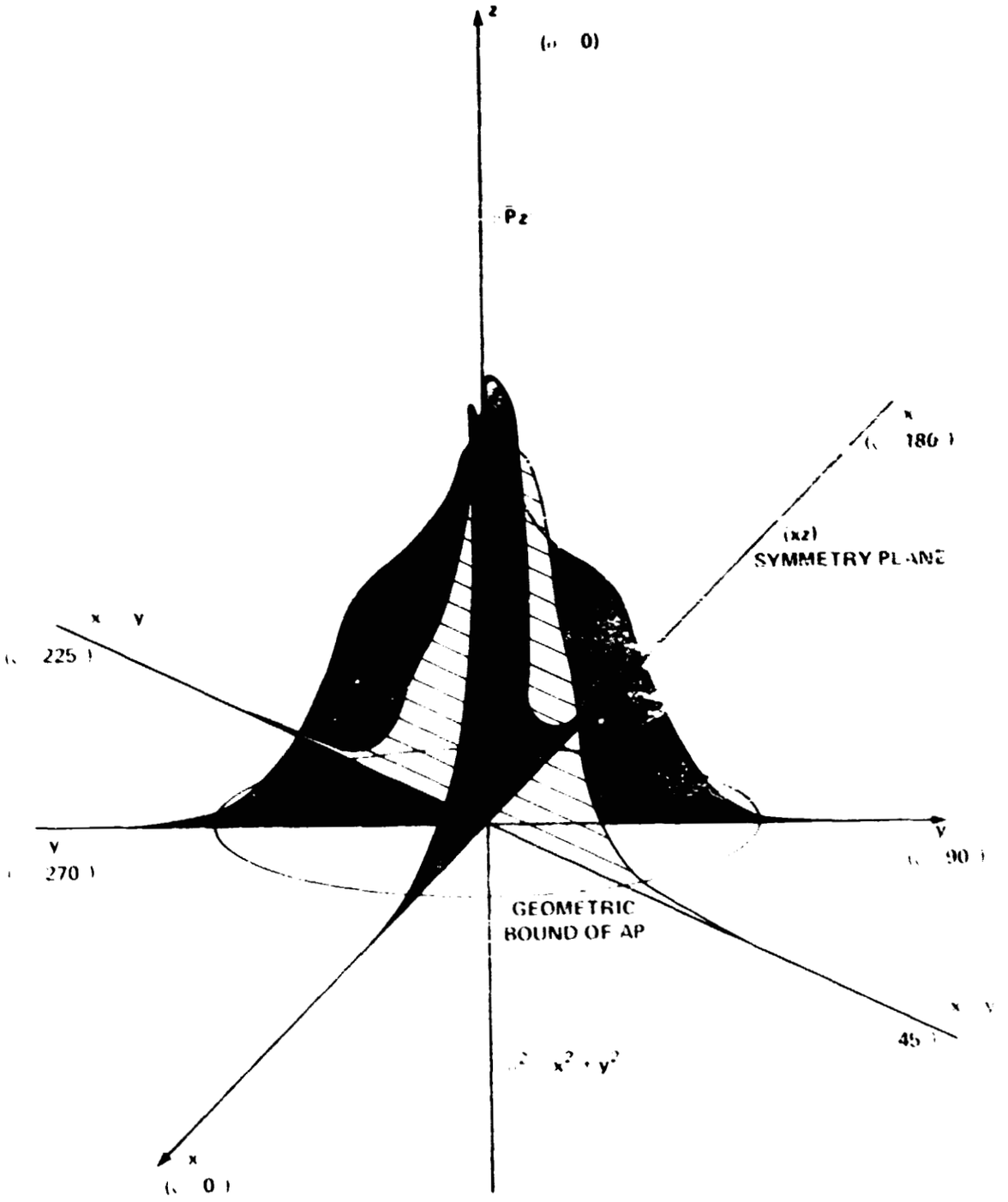

Figure 8. Isometric Representation of Pz at $z = D^2/16\lambda$, N = 20.84.

plots of (P_z) versus (σ) suggested that a selection of the position (x, y, z) of a noise source on a spacecraft (S/C) would be such that, when rotating the radiometer about the x-axis, the incremental noise temperature due to that source could be maximized or minimized. The maximization might correspond to an enhanced calibration procedure, whereas the minimization might correspond to ordinary operation where a noise source to be discriminated against was some structural member on the S/C platform.

ANTENNA NOISE-TEMPERATURE (FRESNEL-REGION)

An estimate of the antenna noise-temperature due to the washer-like noise source at a distance equal to $D^4/16\lambda$ from the aperture, as previously described, can be made using the power-density values of the single (yz-plane) cut of Fig. 4. The washer radii are taken to be (σ_{AP}) and ($\sigma_{AP} - 2\lambda$) for this estimate, so that the latter lies entirely within the geometric bound of the projected aperture. Since $< \overline{P_z} >$ is strongly collimated at $D^2/16\lambda$, the denominator of equation (32) is approximated as follows.

$$\iint_{I} P_z(\sigma, \zeta)\, \sigma\, d\, \sigma\, d\, \zeta \approx \iint_{IV+V} P_z(\sigma, \zeta)\, \sigma\, d\, \sigma\, d\, \zeta \approx (1.5)\left(\frac{\sigma^2}{2}\right)(2\pi)\,\Big|_{0}^{\sigma_{AP}} = 1.5\,\pi\sigma_{AP}^2 \qquad (41)$$

The average value of (P_z) over the washer is taken to be 0.15.

$$\frac{T_A(\sigma, \zeta)}{T_S(\sigma, \zeta)} \approx \frac{0.15[\pi(\sigma_{AP}^2) - \pi(\sigma_{AP} - 2\lambda)^2]}{1.5\pi\,\sigma_{AP}^2} \approx 0.03 \qquad (42)$$

Axial symmetry was assumed for (P_z) in this estimate.

A more precise calculation of (T_A/T_S) was made taking four full cuts ($\Delta\zeta = 45°$) through the Fresnel distribution, and proceeding as in equation (36). The denominator of (32) was evaluated at surface (I), removed (1λ) in the positive ($\hat{i}_z$) direction to obviate any difficulty with singularities ($r = 0$) on the reflector surface, instead of the (xy) or aperture plane. The divergence of $< \overline{P} >$ over the (1λ) distance was assumed to be negligible. The ratio (T_S/T_A) for A_2 in Fig. 9 corresponds to the case estimated previously, and equals (0.037).

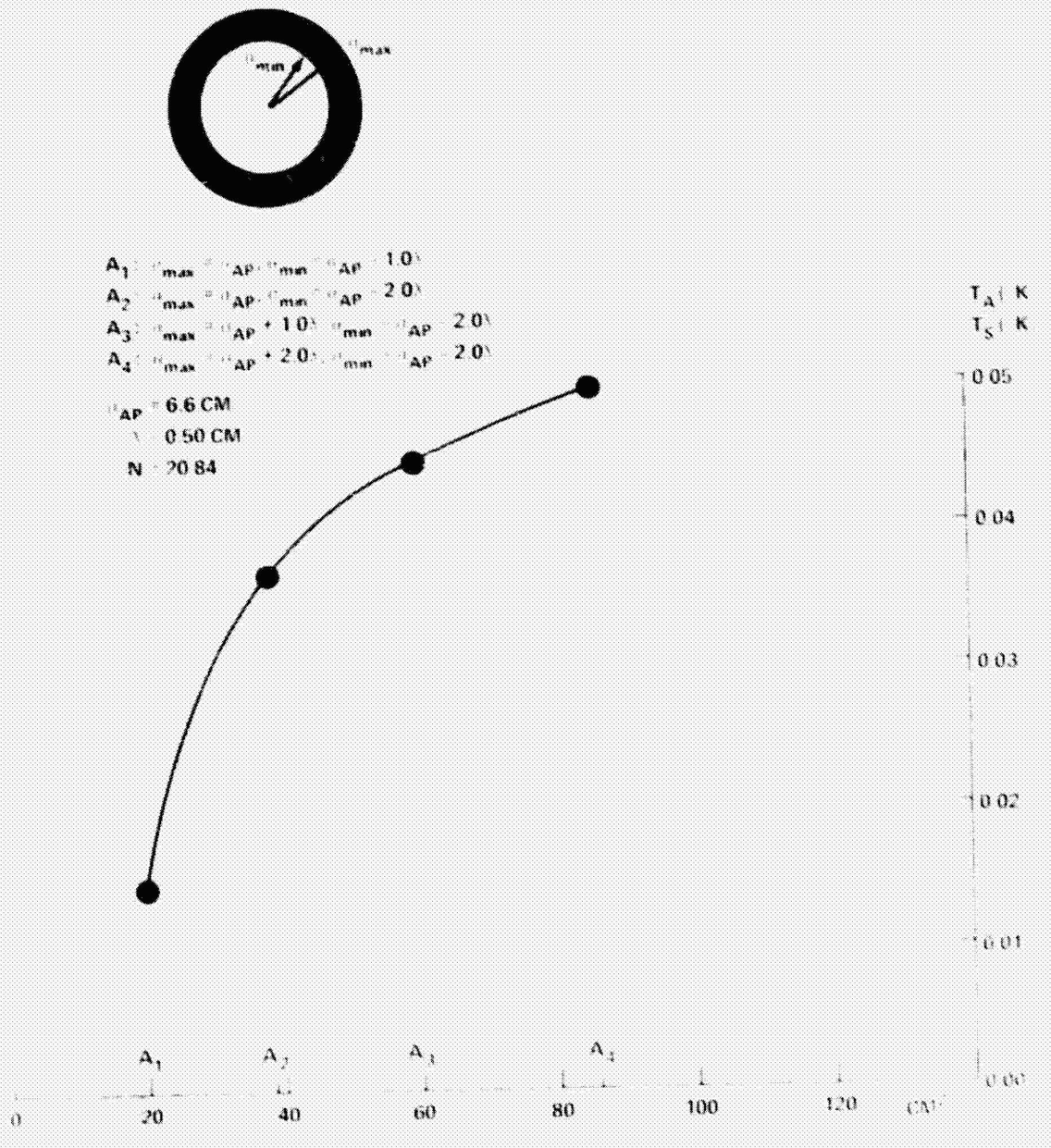

Figure 9. Antenna Noise-Temperature vs. Area of Noise-Source.

ANTENNA NOISE-TEMPERATURE (MULTIPLE/COMPLEX SOURCES)

The convenient symmetry of the abstract noise source used in the preceding calculation of antenna noise-temperature would seldom, if ever, be encountered in a real-world problem. Multiple and complex surface geometries of many types can be found in spacecraft environments or otherwise imagined. It is interesting to consider a few of these in terms of the Poynting formulation and explore their subleties. Figure 10 depicts multiple closed surfaces. The influence of the angle between the normals and the incident Poynting vector can be seen more clearly here than in the preceding calculation, where the angle was approximately ninety-degrees over the flat washer, an "open" surface. Limits of integration on the surfaces (γ_1, γ_2, γ_3) of Figure 10 must necessarily be found after the Poynting vector field has been defined, or calculated, in this first-order approach; interaction between the surfaces is not considered. The noise-temperature formulation for Fig. 10 could be written in terms of open integrals as follows:

$$T_A = \frac{\iint_{\gamma 1 i} T_{s_1} <\bar{P}> \cdot \bar{n}\, ds + \iint_{\gamma 2 i} T_{s_2} <\bar{P}> \cdot \bar{n}\, ds + \iint_{\gamma 3 i} T_{s_3} <\bar{P}> \cdot \bar{n}\, ds}{\iint_{AP} <\bar{P}> \cdot \bar{n}\, ds} \qquad (43)$$

where the notation γ_{1i}, etc., implies that the integration is over that part of γ_1, etc. which is illuminated by the Poynting vector field. The sources (T_s) are functions of (x, y, z).

Equation (43) is actually over a closed surface such as (s_2) in Fig. 2, and closure may be imagined over virtually any surfaces between the limits of integration of the physical surfaces shown in Figure 10. Since these surfaces which establish closure are associated with zero temperature values, they do not appear explicitly in (43). The far-field discussion is not resumed here since the Poynting vector formulation is perfectly general in both Fresnel and Fraunhofer-regions and, as a practical matter, causes no difficulties with respect to core requirements or computer cpu requirements. The scalar or solid angle approach of (18) remains a viable alternative where the noise sources are sufficiently remote with respect to the antenna.

ORIGINAL PAGE
BLACK AND WHITE PHOTOGRAPH

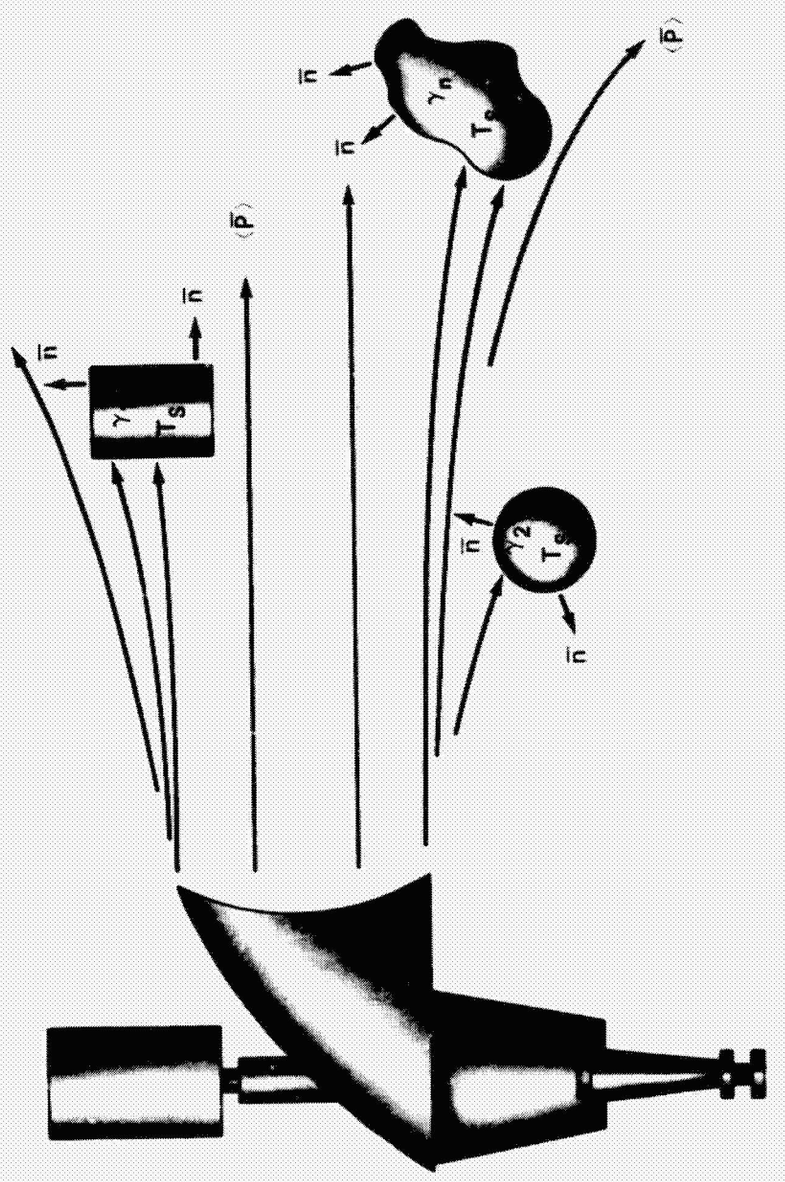

Figure 10. Multiple Closed-Surface Noise Sources.

A possibility not illustrated by Fig. 10, obscuration, is given as Fig. 11. In this first-order simulation scattering around the obstacles has been disregarded. That is, the Poynting vector field which was calculated prior to the introduction of the noise sources is not amended, and a geometric-optics viewpoint is taken upon introduction of the noise sources. Under this simplistic assumption, the upper part of surface (γ_2) is obscured by surface (γ_1) in Fig. 11, and the limits of integration on (γ_2) must be prescribed accordingly.

Many complex situations may arise, including cavities and self-obscuration. Determination of the limits of integration for these will be extremely difficult for general surfaces under the geometric-hypothesis used above. No attempt was made at this writing to treat such examples. They were regarded as lying beyond the scope of first-order antenna noise-temperature calculation.

A few cursory remarks may be useful regarding the divergence region and the Poynting vector formulation. Away from the Fresnel-region, the fields of an antenna such as a paraboloid begin to diverge as the inverse first power of distance, and the Poynting vectors begin to diverge as the inverse second power of distance. See (21). The conservation of energy is implicit here since the area through which power flows orthogonally ($< \overline{P} > \| \overline{n}$) varies directly as the second power of distance, and the picture is one of spherical-wave propagation. For all finite distances from finite reflector antennas the situation described is never fully realized. To some extent the propagation is curvilinear rather than rectilinear. It is possible under such circumstances, for the angles between the normals and the Poynting vectors on surfaces (γ_1) and (γ_2) to differ for "magnified" objects. See Fig. 12, where the unperturbed field of Poynting vectors is assumed and spheres of two sizes are placed, sequentially, in that field. If there is a presumption of curvilinear propagation, two influences may be operative; the set of dot products in (γ_1) may not be replicated (1:1) in γ_2 and (2) $< \overline{P} >$ may not vary inversely with distance squared either, even though area will surely vary directly with distance squared. The effects might compensate or augment to some extent in a given antenna noise-temperature calculation.

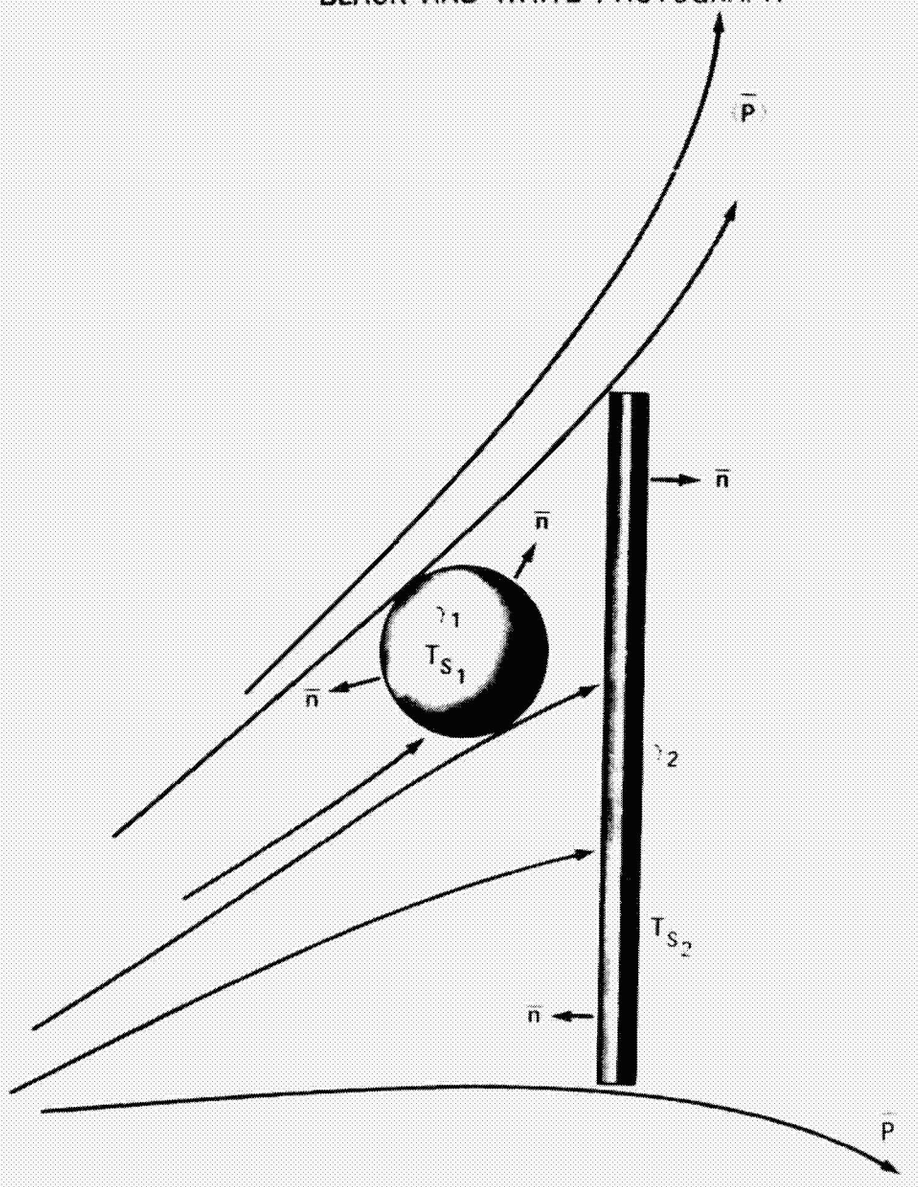

Figure 11. Obscuration Between Closed-Surface Noise Sources of Different Temperature.

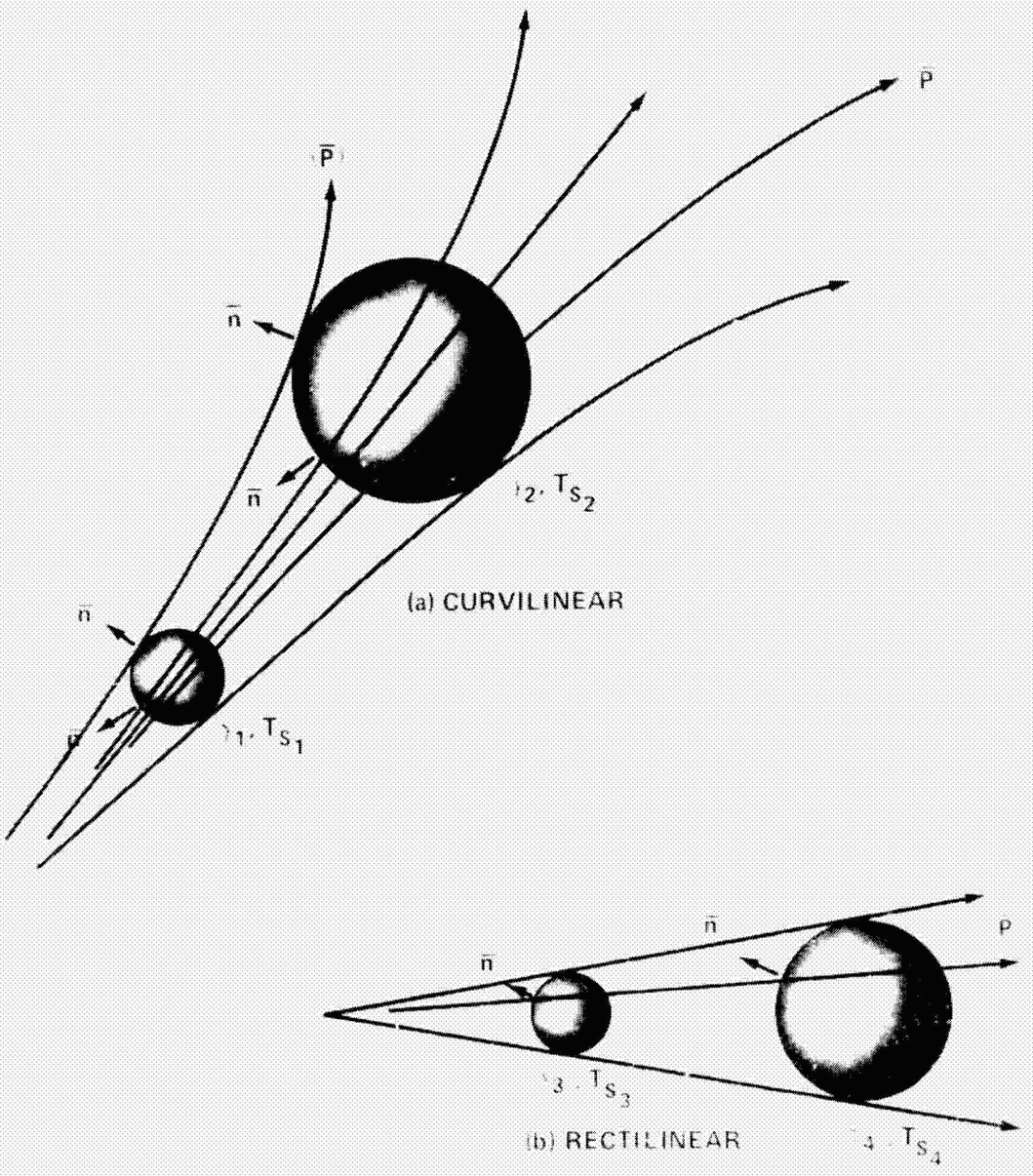

Figure 12. The Divergence Region.

CONCLUSION

This document utilized a time-average Poynting vector formulation for antenna noise-temperature calculations in the Fresnel-region assuming radiation pattern reciprocity. The time-average Poynting vector was computed from the complex scattered electric and magnetic fields and was regarded as a double-projection in space and time so that only synchronous, orthogonal components of the field-pair contributed to the result. Phase information, present in the classic Poynting vector, was suppressed, and a cross-correlation between the coherent time-average vector and incoherent noise-source was performed to obtain antenna noise-temperature values. The spherical surfaces, on which the values for the cross-correlation are assumed to lie in conventional Fraunhofer-region calculations, were deformed to cylindrical shape for the Fresnel-region calculations. Total antenna power was obtained by integrating the time-average Poynting vector over the base of a cylinder, instead of developing the far-field pattern and integrating over 4π steradians of solid-angle, and was identified as an invariant for the problem.

A discussion of the significance of the uniplanar symmetry of the offset paraboloid and the linearly-polarized feed led to a description of the directions and relative magnitudes anticipated in the Fresnel-region. An estimate of antenna noise-temperature was made prior to the introduction of the complete analytical/numerical determination of antenna noise-temperature by means of the computer program. The feed directivity was shown to affect the result. An interpolation scheme was introduced whereby individual cuts of an asymmetric power-density distribution were treated as if axial symmetry existed subject to an averaging process. The ratio of antenna noise-temperature to source temperature $T_A(^\circ K)/T_s(^\circ K)$ was found to lie between 0.014 and 0.050 for the washer-like source whose inner and outer radii departed from the aperture radius by plus/minus two wavelengths. Some dicta was presented for multiple sources and obscuration problems.

ACKNOWLEDGMENTS

The author acknowledges input from the cited references, and helpful discussions and reviews from Dr. J. C. Shiue, R. Meneghini, and Dr. D. M. LeVine of Goddard Space Flight Center. The author is also indebted to Mr. R. Miezis of Sigma Data Services, Inc. for the development of the computer program, the generation of the program-derived Fresnel-region data, and the noise-temperature integrations.

REFERENCES

1. Skolnik, M. I., "Introduction to Radar Systems", McGraw-Hill Book Company, Inc., 1962.
2. Hansen, R. C., "Microwave Scanning Antennas", Vol. I, Apertures, Academic Press, 1964.
3. Stratton, J. A., "Electromagnetic Theory", McGraw-Hill Book Company, Inc., 1941.
4. Silver, S., "Microwave Antenna Theory and Design", McGraw-Hill Book Company, Inc., 1949.
5. Schmidt, R. F., "The Calculation of Electromagnetic Fields by the Kirchhoff-Kottler Method", GSFC-X-525-70-293, May 1970.
6. Schmidt, R. F., "The Calculation of Electromagnetic Fields in the Fresnel and Fraunhofer Regions using Numerical Integration Methods", GSFC-X-811-71-392, July 1971.
7. Paris, D. T. and Hurd, F. K., "Basic Electromagnetic Theory", McGraw-Hill Book Company, Inc., 1969.
8. Fano, R. M., Chu, L. J. and Adler, R. B., "Electromagnetic Fields, Energy, and Forces", The M.I.T. Press, 1968.
9. Papas, C.H., "Theory of Electromagnetic Wave Propagation", McGraw-Hill Book Company, 1965.
10. Kaplan, W., "Advanced Calculus", Addison-Wesley Pub. Co., 1952.
11. Collin, R. R. and Zucker, F. J., "Antenna Theory", McGraw-Hill Book Company, Inc., 1969.
12. Stutzman, W. L., and Thiele, G. A., "Antenna Theory and Design", John Wiley and Sons, 1981.

APPENDIX A

The Electric Field at Infinity

The following development formally establishes the vanishing of the radial $\bar{E}$-field at infinity. Ref. 6. p. 7; or Ref. 10, p. 152 provides the gradient,

$$\nabla\xi = \frac{1}{\alpha}\frac{\partial\xi}{\partial r}\hat{1}_r + \frac{1}{\beta}\frac{\partial\xi}{\partial\theta}\hat{1}_\theta + \frac{1}{\gamma}\frac{\partial\xi}{\partial\phi}\hat{1}_\phi \tag{1-A}$$

$$\alpha = \left|\frac{\partial}{\partial r}(r\hat{1}_r)\right| = 1 \tag{2-A}$$

$$\beta = \left|\frac{\partial}{\partial\theta}(r\hat{1}_r)\right| = r \tag{3-A}$$

$$\gamma = \left|\frac{\partial}{\partial\phi}(r\hat{1}_r)\right| = r\sin\theta, \tag{4-A}$$

in general curvilinear coordinates. Then

$$[(\bar{n}\times\bar{H}_1)\cdot\nabla]\nabla\psi = \left[(\bar{n}\times\bar{H}_1)\cdot\hat{1}_r\frac{\partial}{\partial r}\right]\nabla\psi = [(\bar{n}\times\bar{H}_1)\cdot\hat{1}_r]\frac{\partial^2\psi}{\partial r^2}\hat{1}_r$$
$$= \hat{1}_r\left(-k^2 + 2\frac{jk}{r} + \frac{2}{r^2}\right)\psi[(\bar{n}\times\bar{H}_1)\cdot\hat{1}_r], \tag{5-A}$$

where

$$\psi = \frac{e^{-jkr}}{r}, \tag{6-A}$$

and

$$\nabla\psi = -\left(jk + \frac{1}{r}\right)\psi\hat{1}_r.$$

The sum of the radial $\bar{E}(x', y', \cdot')$ field components, neglecting higher-order terms is, therefore.

$$\frac{1}{4\pi}\int_{s_1}\left(\frac{-k^2}{j\omega\epsilon} - j\omega\mu\right)\psi(\bar{n}\times\bar{H}_1)\cdot\hat{1}_r\,ds = 0, \tag{7-A}$$

since

$$k^2 = \omega^2\mu\epsilon. \tag{8-A}$$

APPENDIX B

Equations for the Offset Paraboloid

Figure B-1 shows the antenna geometry used in this document The equations for the surface and certain other computer inputs are given below.

A convenient parametric form for the equations of an offset paraboloid expresses coordinates on a parent paraboloid, whose vertex lies on the $\hat{1}_z$ axis, in terms of a radial variable (σ_{1P}) emanating from a local or offset-paraboloid generating axis and an azimuthal variable (ζ_{1P}).

$$x_P = \sigma_{1P} \sin \zeta_{1P} + x_{1P}, \qquad x_{1P} < 0 \tag{1-B}$$

$$y_P = -\sigma_{1P} \cos \zeta_{1P} + y_{1P}, \qquad y_{1D} \equiv 0 \tag{2-B}$$

$$z_P = \frac{\sigma_P^2}{4F} + z_{1P}, \qquad z_{1P} = -F \tag{3-B}$$

$$\sigma_P^2 = x_P^2 + y_P^2 \tag{4-B}$$

The mid-point of the circular (projected) aperture of the offset paraboloid can be situated at the origin of coordinates, as shown in Fig. B-1, by a simple translation. Then

$$x_{PT} = x_P + x_T, \qquad x_T = -x_{1P} \tag{5-B}$$

$$y_{PT} = y_P + y_T, \qquad y_T \equiv 0 \tag{6-B}$$

$$z_{PT} = z_P + z_T, \qquad z_T = -z_{P_{max}} = \frac{-(-\sigma_{1P_{max}} + x_{1P})^2}{4F} + F \tag{7-B}$$

It follows that

$$x_{PT} = \sigma_{1P} \sin \zeta_{1P} \tag{8-B}$$

$$y_{PT} = -\sigma_{1P} \cos \zeta_{1P} \tag{9-B}$$

$$z_{PT} = \frac{\sigma_P^2 - (\sigma_{1P_{max}} + x_{1P})^2}{4F} \qquad (10\text{-B})$$

$$\sigma_P^2 = x_P^2 + y_P^2 \qquad (4\text{-B}), (11\text{-B})$$

Parameters for the radiometer geometry of Fig. B-1 are

$F = 0.26' = 7.92\,cm$	focal length
$\sigma_{max} = 0.2165' = 6.60\,cm$	maximum aperture radius
$\sigma_0 = 0.0' = 0.0\,cm$	minimum aperture radius
$x_{1P} = -0.548' = -16.7\,cm$	x-offset
$y_{1P} = 0.0' = 0.0\,cm$	y-offset
$z_{1P} = -F = -0.26' = -7.92\,cm$	(O, F) congruence
$x_T = 0.548' = 16.7\,cm$	x-translation of AP
$y_T = 0.0' = 0.0\,cm$	y-translation of AP
$z_T = -0.30198' = -9.20\,cm$	z-translation of AP
$\lambda = 0.01639'$ (0.50 cm)	wavelength
$f = 60.0\,GHz$	frequency
LI = 0.5	sampling interval (max.) on surface
SIGN = 1.0	control parameter
S = 1.0	feed strength or weight
$\psi = 0.0°$	feed initial phase
P(I) = 1.0, P(J) = P(K) = 0.0	Cartesian polarization moments for feed
$x_\epsilon = 0 + x_T$	x-feed position
$y_\epsilon = 0 + y_T$	y-feed position
$z_\epsilon = 0 + z_T$	z-feed position
$\alpha = \beta = 90.0°, \gamma = 0.0°$	Eulerian angles for feed
N = 20.84 or N = 0.0	feed exponents for −15 dB or 0 dB source-taper (w/o space divergence)

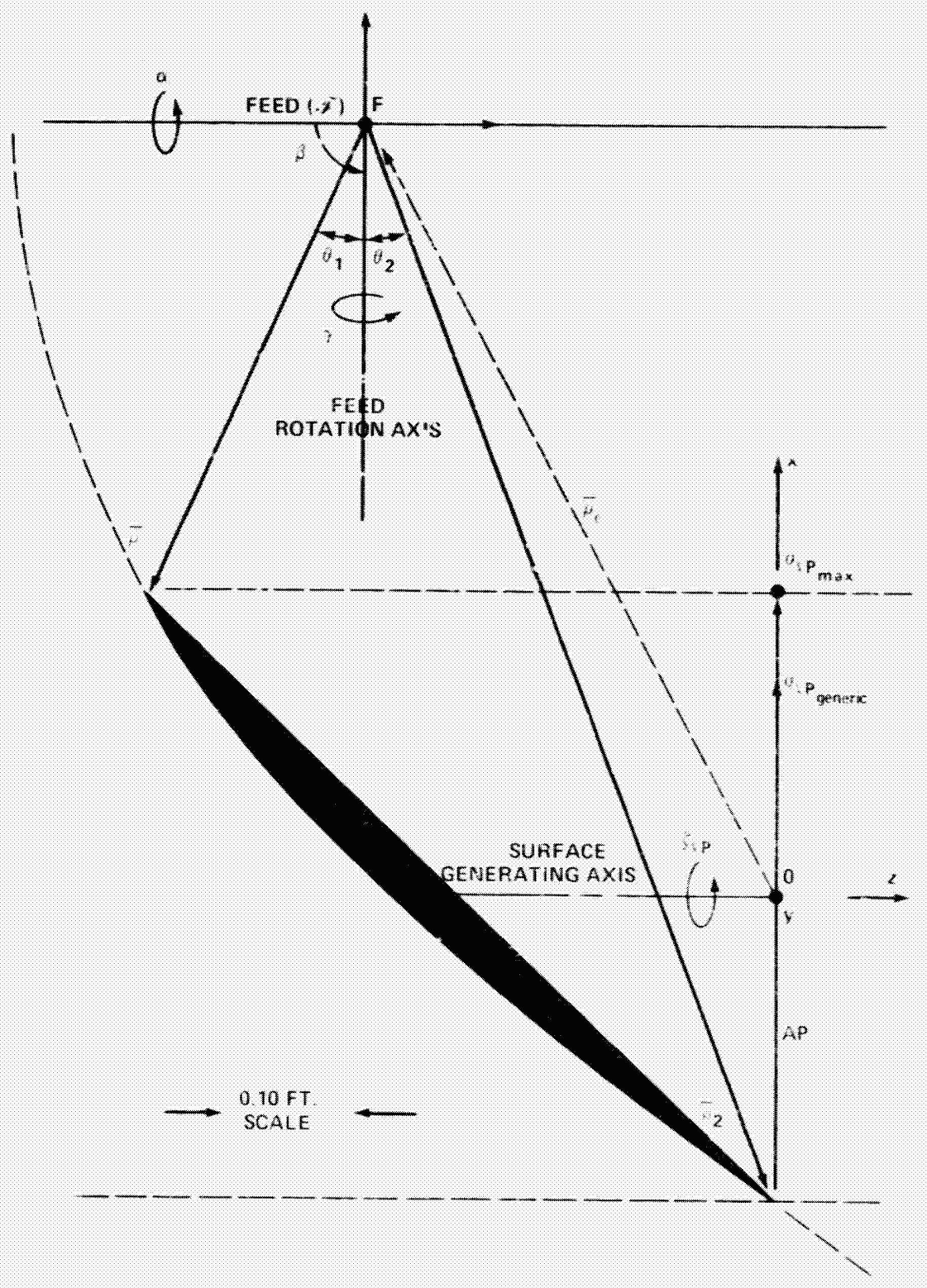

Figure B-1. The 13.2 cm Offset Paraboloid.